Bioactive Materials 15 (2022) 173–184

Contents lists available at ScienceDirect

Bioactive Materials

journal homepage: www.keaipublishing.com/en/journals/bioactive-materials

Eco-friendly bacteria-killing by nanorods through mechano-puncture with top selectivity

Jing Ye [a,1], Bo Li [a,1], Yufeng Zheng [b], Shuilin Wu [c], Dafu Chen [d], Yong Han [a,*]

[a] State Key Laboratory for Mechanical Behavior of Materials, Xi'an Jiaotong University, Xi'an, 710049, China
[b] Center for Biomedical Materials and Tissue Engineering, Academy for Advanced Interdisciplinary Studies, Peking University, Beijing, 100871, China
[c] School of Materials Science & Engineering, The Key Laboratory of Advanced Ceramics and Machining Technology by the Ministry of Education of China, Tianjin University, Tianjin, 300072, China
[d] Laboratory of Bone Tissue Engineering, Beijing Research Institute of Traumatology and Orthopaedics, Beijing Jishuitan Hospital, Beijing, 100035, China

ARTICLE INFO

Keywords:
Anti-bacteria
Nanorods
Top sharpness
Mechano-puncture
Finite element simulation

ABSTRACT

Nanorods can induce mechano-puncture of *Staphylococcus aureus* (*S. aureus*) that often impairs osseointegration of orthopedic implants, while the critical nanorod top sharpness able to puncture *S. aureus* and the predominant contributor between top sharpness and length to mechano-puncture activity remains elusive. Herein, we fabricated three kinds of Al_2O_3-wrapped nanorods patterned arrays with different lengths and top sharpness. The top-sharp nanorods have lengths of 469 and 884 nm and the shorter show a length identical to the top-flat nanorods. Driven by the equivalent adhesive force of *S. aureus*, the top-flat nanorods deform cell envelops, showing a bacteriostatic rate of 29% owing to proliferation-inhibited manner. The top-sharp nanorods puncture *S. aureus*, showing a bactericidal rate of 96% for the longer, and 98% for the shorter that simultaneously exhibits fair osseointegration in bacteria-infected rat tibias, identifying top sharpness as a predominate contributor to mechano-puncture activity. Based on finite-element simulation, such top-flat nanorod derives the maximum stress (S_{max}) of 5.65 MPa on cell wall, lower than its ultimate-tensile-strength (13 MPa); while such top-sharp and shorter nanorod derives S_{max} of 20.15 MPa to puncture cell envelop. Moreover, a critical top conical angle of 138° is identified for nanorods able to puncture *S. aureus*.

1. Introduction

Bacterial colonization and biofilm formation derived infection is the major cause for failure of orthopedic implants [1,2]. To solve the problem, preventing bacteria from adhesion to the implant surfaces and killing bacteria are currently used strategies, and the latter is proven to be more highly effective for anti-bacteria [1]. Prevalently, chemical bactericides, such as antibiotic [3–5], bactericidal ions [6–9] and antimicrobial peptide [10] were loaded on the implant surfaces to kill bacteria *via* inhibiting bacterial wall synthesis and disrupting DNA replication [11,12] or to destruct cell envelop (consisting of cell wall and membrane) *via* inducing reactive oxidation species (ROS) [6,9]. However, these bactericides are likely able to induce cytotoxicity [9,13] to impair osseointegration, nephrotoxicity [14] or neurovirulence [15], and render multi-drug resistance bacteria or superbacteria [2,11], limiting their use and effectiveness in implants for orthopedic repair. In addition, photosensitizer incorporated coatings are widely investigated to realize antibacterial activity utilizing their photo-thermal/dynamic effects [16–19]. Nevertheless, photo-thermal effect derived hyperpyrexia and photodynamic effect derived ROS may destroy peri-implant healthy tissues [20], moreover, the incorporated photosensitizers also may induce biotoxicity [21].

Inspired by the nanorods-patterned arrays of cicada and dragonfly wings that show bactericidal effect [22], diverse nanoscaled arrays with high length/diameter ratio, such as Si [23,24] and polymer [25] nanofibers, TiO_2 and ZnO nanorods [26,27], and carbon nanotubes [28], which are in follows collectively termed as nanorods, have been constructed and proven to mechanically kill bacteria. It is clear that when cultured on nanorods, bacteria subject to bacterial gravity, van der Waals force and the adhesive force derived by bacteria-secreted

Peer review under responsibility of KeAi Communications Co., Ltd.
* Corresponding author.
E-mail address: yonghan@mail.xjtu.edu.cn (Y. Han).
[1] J. Ye and B. Li contributed equally to this work.

https://doi.org/10.1016/j.bioactmat.2021.11.028
Received 25 October 2021; Received in revised form 25 November 2021; Accepted 25 November 2021
Available online 21 December 2021

extracellular polymeric substance (EPS) [2,29–32], among which the EPS-derived adhesive force is much stronger than the former [31,32]. This adhesive force would not only induce shear force acting on cell envelop of bacteria to limit their migration over the nanorods, but also drive the nanorods to induce cell envelop deformation (mechano-deformation) or even to penetrate into the envelop (mechano-puncture) [31,33]. Given that gram-negative bacteria have thinner cell wall than gram-positive bacteria, the gravity and van der Waals force induced stretching force is only able to rupture cell envelops of gram-negative bacteria [2,34], while the EPS-derived strong adhesive force can draw nanorods to penetrate into both gram-negative and positive bacteria, leading to their death [26,27,35]. Therefore, coating nanorods patterned arrays with mechano-puncture ability is expected to protect orthopedic implants more effectively from bacteria-derived infection, which is predominately caused by *Staphylococcus aureus* (*S. aureus*) owing to its gram-positive and antibiotics-resistant feature [36,37].

Given that the mechano-puncture ability of nanorods-shaped arrays against *S. aureus* depends on their topographical parameters, especially on the nanorod top sharpness [37,38], various nanorods with different top sharpness were fabricated but exhibit distinct mechano-puncture efficiency. For instance, top-flat Si nanorods were unable to penetrate into *S. aureus* [24], while top-blunt TiO_2 nanorods shallowly penetrated into *S. aureus* with an antibacterial rate of ~10% [26]. Encouragingly, top-sharp Si nanorods were shown to deeply penetrate into *S. aureus* to effectively kill them [23]. Although these works qualitatively suggest that the mechano-puncture activity of the arrays is enhanced with sharpening of nanorod top, the concentrated stress on cell envelop derived by the nanorods with different top sharpness have not been quantified yet, leading to uncertainty of the critical nanorod top sharpness able to penetrate into *S. aureus*. In addition to top sharpness, nanorod length is also found to contribute to mechano-puncture efficacy [28,38], but the drawn results are contradictive. For instance, carbon nanotubes with lengths of 1 and 30 μm killed ~67% and ~17% of the attached *S. aureus*, respectively [28]. Contrarily, longer Si nanorods with sharp tops exhibited more pronounced bactericidal activity compared to the shorter ones with slightly blunt tops [38]. The reason for this controversy is that the topographical parameters, e.g. top sharpness and length of the nanorods patterned arrays in these works are concomitantly but not independently changed with each other [1,2,34,38]. These concomitant changes draw another confusion that for top sharpness and length, which is the predominate contributor to mechano-puncture activity of the nanorods. Notably, the variation of topographical parameters of the arrays is also accompanied with the changes in surface roughness, hydrophilia and zeta potential, which also influence bactericidal activity [2].

Herein, we constructed three kinds of core-shell structured nanorods patterned arrays on Ti discs, with micro-arc oxidation (MAO) and hydrothermal growth (HG) formed hydroxyapatite (HA) or ZnO as a core and atomic layer deposition (ALD) formed amorphous Al_2O_3 as a shell (schematically as Fig. 1a). The arrays exhibit two kinds of different nanorod top sharpness: flat top and sharp top, in which the top-sharp nanorods reveal two kinds of lengths and the short show an equivalent length to the top-flat nanorods. With these nanorods patterned arrays, we identify the critical top sharpness of nanorods able to penetrate into *S. aureus* and clarify the contributions of nanorod top sharpness and length to mechano-puncture derived bactericidal efficiency, providing the quantitative basis to optimize the top sharpness for achieving mechano-puncture. We also show that the top-sharp and short nanorods patterned array acts on *S. aureus via* unique mechano-puncture without impairing the viability of mesenchymal stem cells (MSCs), having an *in vitro* and *in vivo* antibacterial rate of more than 98%, and simultaneously exhibits fair osseointegration in *S. aureus*-infected rat tibia. Such antibacterial efficiency is comparable to that exhibited by the synergistic action of nanorods-derived mechano-puncture, bactericidal components and/or photo-thermal/dynamic effect [27,39,40].

2. Experimental sections

2.1. Fabrication of nanorods patterned arrays

HA nanorods-patterned array was fabricated using MAO and hydrothermal treatment (HT), the detailed process was described in our previous work [41]. Briefly, Ti discs with size of 14 × 2 mm were micro-arc oxidized (MAOed) in an aqueous electrolyte containing calcium acetate (0.2 M) and β-glycerophosphate disodium (0.02 M) at an applied voltage of 400 V, a pulse frequency of 100 Hz and a duty ratio of 26% for 3 min. After adding 10 ml NaOH solution (0.01 M) into 60 ml volumetric Teflon-lined autoclave, each of the resultant MAOed Ti discs was immersed in the NaOH solution to receive HT at 140 °C for 24 h, consequently to form the HA nanorods-patterned array.

Commercial pure Ti discs with size of 14 × 2 mm were MAOed in zinc acetate (0.2 M) contained aqueous electrolyte at an applied voltage of 530 V, a pulse frequency of 100 Hz and a duty ratio of 26% for 1 min. Each MAOed Ti disc underwent HT in 10 mL NaOH solution (0.01 M) at 140 °C for 2 h or 4 h to form the differently longitudinal ZnO nanorods-patterned arrays.

All the resultant nanorods-arrayed Ti discs were cleaned with deionized water and dried in an oven overnight at 60 °C.

2.2. Al–O layers deposition on the nanorods and Ti by ALD

An ALD equipment (F-100-41, MNT Micro and Nanotech Co., LTD, China) was used to coat Aluminum (Al) and Oxygen (O) (Al–O) layers on the as-formed nanorods-patterned arrays. Trimethylaluminum and hydrogen peroxide (H_2O_2, 40 vol%) aqueous solution were used as precursors of Al and O, respectively, and high-purity N_2 was used as the purged gas. The nanorods patterned Ti discs were put into chamber of the ALD equipment, followed by vacuating the chamber to 10^{-3} Pa and heating the chamber up to 150 °C. Subsequently, Al and O precursors and N_2 were sequentially auto-injected into the chamber following the sequence of 1 s TMA expose/20 s N_2 purge/0.2 s H_2O_2 expose/40 s N_2 purge for each deposition cycle. After 100 deposition cycles, Al–O coated nanorods patterned arrays were obtained. In addition, an Al–O layer was deposited on Ti disc using the aforementioned ALD procedure, followed by annealing at 800 °C for 4 h at atmosphere. The as-deposited and annealed Al–O layers on Ti discs were used to identify phase component in the ALD-derived Al–O layer.

2.3. Structural analysis of the nanorods patterned arrays

Phase identification was carried out with an X-ray diffractometer (XRD, X'Pert PRO, Netherland) in θ-2θ geometry using Cu-Kα (λ = 0.15406 nm) radiation over a 2θ angles of 20–60° at a step of 0.02° with 40 kV scanning voltage and 40 mA scanning current, and the phases from obtained XRD spectra were identified by the ICDD cards. Field emission scanning microscope (FE-SEM, FEI QUANTA 600F, U.S.A.) was used for examining the morphologies of the nanorods patterned arrays before and after deposition of ALD-derived Al–O layers. The nanorods scratched from Al–O coated nanorods patterned arrays were examined by transmission electron microscope (TEM, JEOL JEM-2000FX, Japan) equipped energy-dispersive X-ray (EDX) operating at 200 kV. The roughness of the Al–O coated nanorods patterned arrays was examined by atomic force microscopy (AFM, SPM-9500J3, Japan).

2.4. Property characterizations of the Al–O coated nanorods patterned arrays

The detailed methods are presented in Supporting information, and all the procedures of animal experiments has been approved by the Institutional Animal Care and Use Commit-tee (IACUC) of Xi'an Jiaotong University.

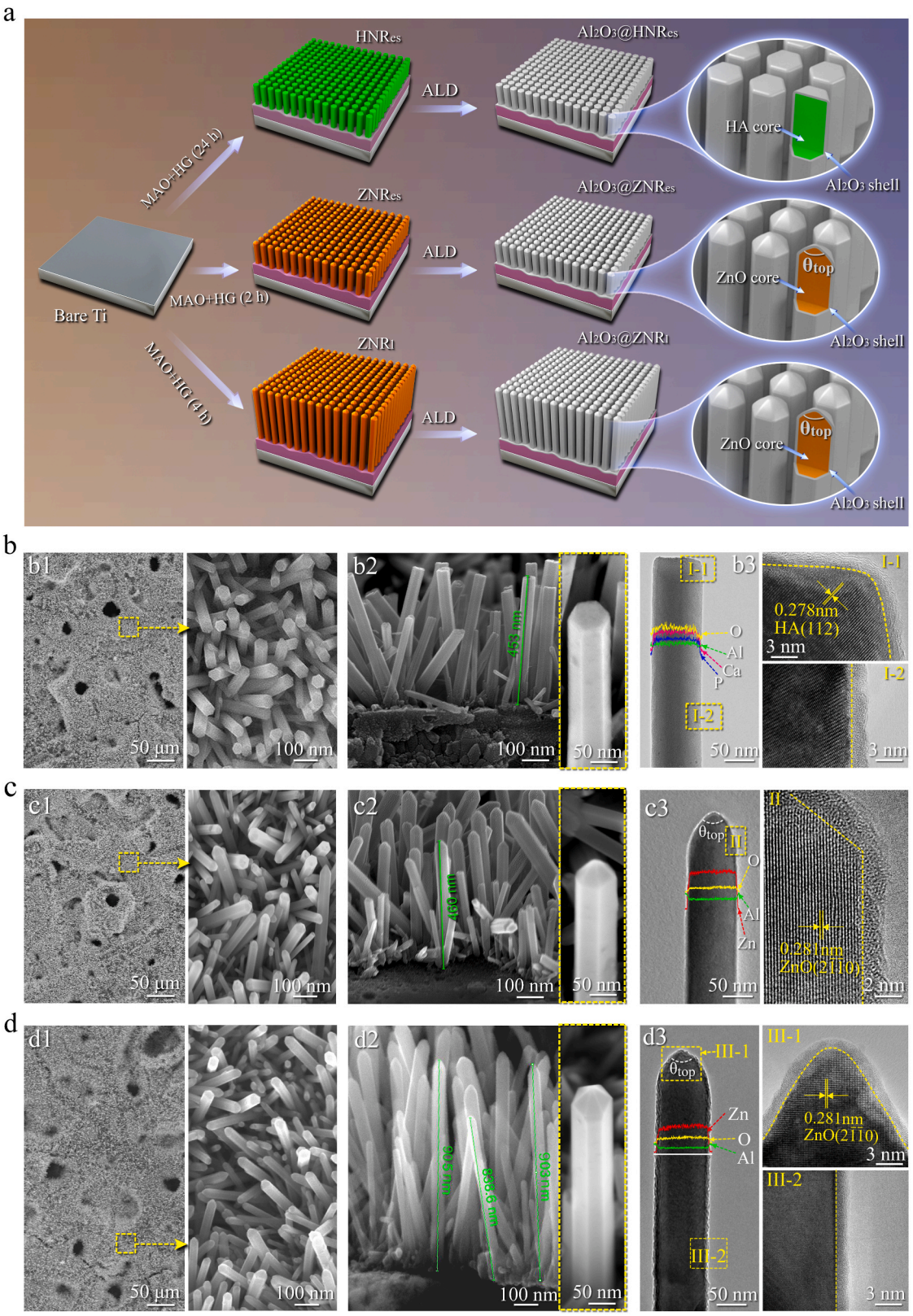

Fig. 1. (a) Schematic illustration of the fabrication process for the nanorods patterned arrays on Ti (θ_{top}: conical angle of nanorod); SEM and TEM analyzed microstructures of (b) Al_2O_3@HNR_{es}, (c) Al_2O_3@ZNR_{es} and (d) Al_2O_3@ZNR_I: (b1, c1 and d1) and (b2, c2 and d2) showing SEM surface and cross-sectional images of the nanorods patterned arrays, respectively; (b3, c3 and d3) showing TEM analyzed the ultrafine structures of individual nanorods scratched from Al_2O_3@HNR_{es}, Al_2O_3@ZNR_{es} and Al_2O_3@ZNR_I, respectively; for the detailed structures of the nanorods, I-1 and I-2 showing the HRTEM images of the square-dotted micro-regions in (b3), II showing the HRTEM image of the square-dotted micro-region in (c3), and III-1 and III-2 showing the HRTEM images of the square-dotted micro-regions in (d3).

2.5. Finite element simulation

The nephograms of stress distribution on cell walls of bacteria induced by top-flat and top-sharp Al–O coated nanorods patterned arrays were drawn through finite element (FE) simulation using Dynaform software (ETA, U.S.A.). The parameters used in our FE model included the thickness, Young's modulus and ultimate tensile strength (UTS) of *S. aureus* cell wall, internal hydrostatic pressure of *S. aureus*, the applied force of nanorod to cell wall and the conical angle (θ_{top}) of nanorod, which were detailedly described in the section of results and discussion, and the critical θ_{top} of nanorods was identified using dichotomy by the Optimization module integrated in the Isight software (Engineous, U.S.A).

2.6. Statistical analysis

The data were expressed as mean ± standard deviation (SD) from repeated independent experiments. The data were analyzed using SPSS 16.0 software (SPSS, U.S.A.). One-way ANOVA followed by a least-significant-difference (LSD) post hoc test was used to determine the level of significance. Here, $p < 0.05$ and 0.01 were considered to be significant and highly significant, respectively.

3. Results and discussion

3.1. The components and structures of the nanorods patterned arrays on Ti substrates

As shown in Figs. S1a and c, the HG formed nanorods on the MAO of Ti disc are composed of HA with a length of 459.9 ± 17.9 nm. This HA nanorods-arrayed coating on Ti disc is bilayer structured, comprising an inner layer of TiO_2 and an outer layer of HA nanorods with flat tops. Likewise formed with MAO and HG, ZnO nanorods-arrayed coatings on Ti discs with two kinds of nanorod lengths also exhibit a bilayer structure, consisting of TiO_2 as an inner layer and ZnO nanorods as an outer layer. Notably, the ZnO nanorods appear hexagonal pyramid shaped on tops (Figs. S1b and S1c). Moreover, the shorter ZnO nanorods show a length of 467.1 ± 15.5 nm, equal to that of the HA nanorods, termed as ZNR_{es} and so did the HA nanorods as HNR_{es}, while the longer ZnO nanorods have a length of 882 ± 20.3 nm, namely ZNR_l.

Aluminum and oxygen atoms were atomic layer deposited as an Al–O ultrathin layer to wrap each nanorod of HNR_{es}, ZNR_{es} and ZNR_l arrays. As shown in Fig. 1b–d, the SEM images reveal that the core-shell structured nanorods in the three arrays align perpendicularly or quasi-vertically to Ti substrates with an interrod spacing of ~80 nm and a dimeter of ~70 nm, and reveal almost identical lengths and top shape to the corresponding primitive nanorods. The high-resolution TEM (HRTEM) images and EDX profiles show that the Al–O layer around each nanorod of HNR_{es}, ZNR_{es} and ZNR_l arrays is uniform in thickness with a value of ~1.5 nm but lack of lattice fringe. Further identification by XRD spectra before and after annealing confirms that the Al–O layer consists of amorphous Al_2O_3 (Fig. S2a). Collectively, the amorphous Al_2O_3-wrapped nanorods are referred to as Al_2O_3@HNR_{es}, Al_2O_3@ZNR_{es} and Al_2O_3@ZNR_l, respectively, in which both Al_2O_3@ZNR_{es} and Al_2O_3@ZNR_l appear hexagonal pyramid shaped on tops with a conical angle θ_{top} of 50°, while Al_2O_3@HNR_{es} are flat on tops with a θ_{top} of 180°, having a nanorod length (~462 nm) identical to Al_2O_3@ZNR_{es} (~469 nm) but almost a half of Al_2O_3@ZNR_l (~884 nm).

3.2. Surface features, Zn^{2+} released from the core-shell structured nanorods patterned arrays and ROS formation on these arrays

Given that surface features such as roughness [42,43], wettability [44,45] and zeta potentials [46,47] can modulate bacterial behaviors, in this context, they were tested on the three kinds of arrays as shown in Fig. 2a–c. Owing to the identical surface morphologies (Fig. 1b1-d1), Al_2O_3@HNR_{es}, Al_2O_3@ZNR_{es} and Al_2O_3@ZNR_l arrays show almost equivalent values of average roughness (Ra) and root mean square roughness (R_q) measured with AFM (Table S1), moreover, contact angle and zeta potential of these arrays are also identical. It is suggested that the variations in nanorod length and top shape of the Al_2O_3-wrapped arrays do not induce the changes in these three parameters of surface features, excluding their contributions to the difference in antibacterial abilities of the arrays.

Excess Zn^{2+} ions released from ZnO nanorods [27] and Zn^{2+}-containing TiO_2 coating [6] are known to disturb metabolic process of bacteria [27], and also enhance intracellular ROS level [6], leading to bacteria death. Moreover, ROS generated on ZnO nanorods [27] and

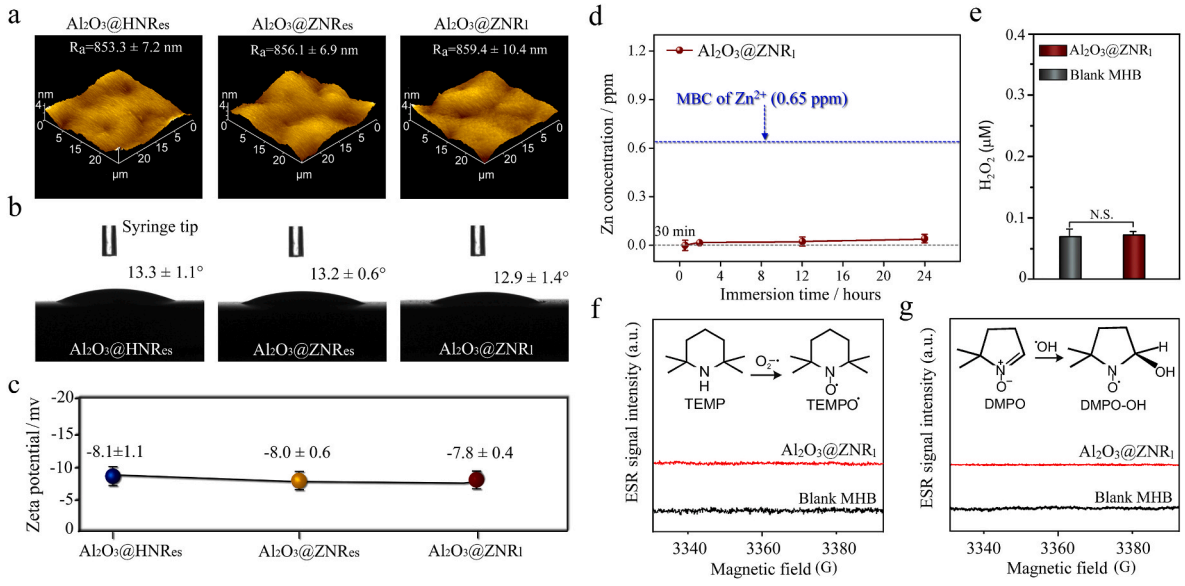

Fig. 2. (a) AFM images, (b) contact angles of water droplets and (c) zeta potentials of Al_2O_3@HNR_{es}, Al_2O_3@ZNR_{es} and Al_2O_3@ZNR_l; (d) Zn^{2+} concentrations of the bacterial culture medium, Mueller Hinton Broth (MHB) immersing Al_2O_3@ZNR_l as a function of immersion time (MBC: minimum bactericidal concentration); (e) the concentrations of H_2O_2 in the blank MHB and MHB immersing Al_2O_3@ZNR_l (N. S.: no significance); the ESR spectra of (f) superoxide (O_2^{-}•) and (g) hydroxyl radical (•OH) in the MHB immersing Al_2O_3@ZNR_l as detected with TEMPO • and DMPO-OH spin trap agents.

Zn^{2+}-containing TiO_2 coating [6] in bacteria culturing medium have been reported to destroy cell envelop integrity of bacteria [27], and also upregulate intracellular ROS level to aggravate damage of cell envelop [6]. Although the nanorods made up of ZnO were demonstrated to have a mechano-puncture effect on bacteria [27], this effect induced bactericidal activity is undistinguishable owing to the concomitant Zn^{2+} and ROS induced bactericidal effect [6,27]. In this context, Zn^{2+} release from and ROS (including superoxide (O_2^-•), hydroxyl radical (•OH) and H_2O_2) formation on both the Al_2O_3-coated ZNR_l and ZNR_{es} arrays were tested in bacterial culture medium, Mueller Hinton Broth (MHB), together with blank MHB as a negative control. As shown in Fig. 2d–f (picking up from Al_2O_3@ZNR_l as a representative), the Zn^{2+} ions released from Al_2O_3@ZNR_l within 24 h of immersion are rare, far less than the minimum bactericidal concentration (MBC) of Zn^{2+}. Moreover,

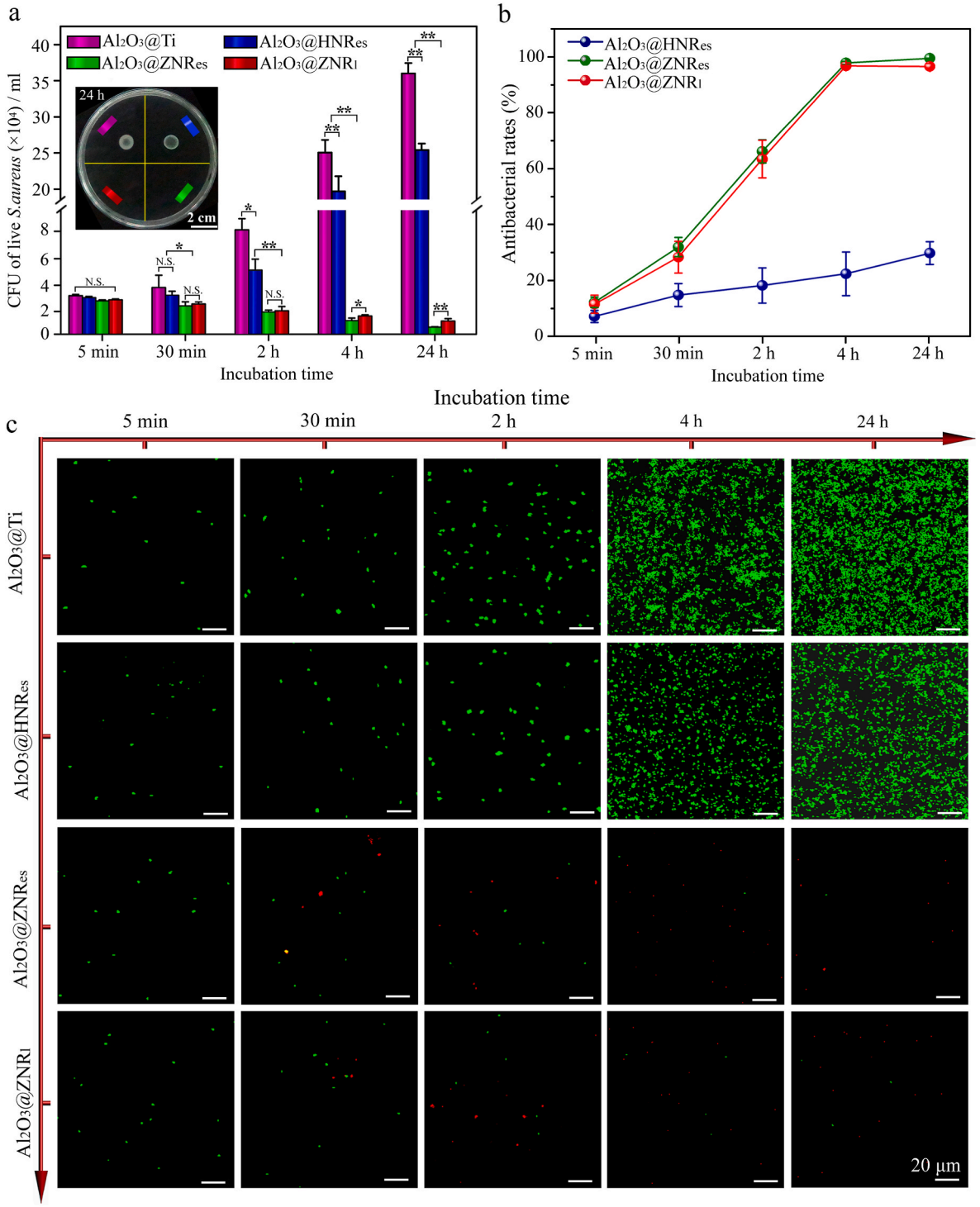

Fig. 3. (a) Numbers of undiluted bacteria colonies formed by dissociating *S. aureus* from Al_2O_3@Ti, Al_2O_3@HNR_{es}, Al_2O_3@ZNR_{es} and Al_2O_3@ZNR_l after different incubation time and then re-cultivating on agar for 24 h, along with the inserted optical photograph of undiluted bacteria colonies formed by dissociating *S. aureus* from the samples after 24 h of incubation and then re-cultivating on agar for 24 h (*$p < 0.05$, **$p < 0.01$, N. S.: no significance); (b) antibacterial rates of the nanorods patterned arrays at different incubation time points; (c) fluorescent live/dead straining images of *S. aureus* cultured on Al_2O_3@Ti and the arrays for different time.

H_2O_2 content of the MHB immersing Al_2O_3@ZNR_l is similar to that of blank MHB, while ESR adsorption peaks of O_2^-• and •HO are invisible for the Al_2O_3@ZNR_l immersed MHB. The results indicate that the ALD-derived amorphous Al_2O_3 ultrathin shells can almost completely inhibit release of ions from the inner cores (such as Zn^{2+} from ZnO and extendedly Ca^{2+} and PO_4^{3-} from HA) and ROS formation on the coated ZNR_l and ZNR_{es} arrays, and amorphous Al_2O_3 does not induce ROS formation by itself. Further, Al_2O_3@HNR_{es}, Al_2O_3@ZNR_{es}, and Al_2O_3@ZNR_l arrays were examined for the intracellular ROS levels of the adhered bacteria, and no elevated intracellular ROS levels appear compared to that displayed by the bacteria adhered on Ti as a negative control (Fig. S3). Also, amorphous Al_2O_3 exhibits the same bacterial adhesion and proliferation as planar Ti (Figs. S2b and c), thus lack of antibacterial activity, because Ti is known to be without antibacterial ability [6]. Therefore, the follows presented difference in antibacterial activities of Al_2O_3@HNR_{es}, Al_2O_3@ZNR_{es} and Al_2O_3@ZNR_l arrays is not owing to chemical contribution.

3.3. Antibacterial activities of the core-shell structured nanorods patterned arrays

The plate-counting assessed bacterial colonies formed by dissociating *S. aureus* from the Al_2O_3-coated nanorods patterned arrays together with Al_2O_3 coated planar Ti (Al_2O_3@Ti) and re-cultivating on agar are shown in Fig. 3a. The bacterial colony numbers (BCNs) increase but with different increments on Al_2O_3@HNR_{es} and Al_2O_3@Ti, while decrease on Al_2O_3@ZNR_{es} and Al_2O_3@ZNR_l with incubation from 30 min to 24 h. In details, at 5 min, the three kinds of Al_2O_3-coated nanorods patterned arrays display a comparable BCN to Al_2O_3@Ti. At 30 min, top-sharp Al_2O_3@ZNR_{es} and Al_2O_3@ZNR_l arrays show significantly decreased BCNs compared to top-flat Al_2O_3@HNR_{es} array that has an equal BCN to Al_2O_3@Ti. Since then, the top-sharp arrays exhibit more pronounced decrease in BCN compared to the top-flat array. Notably, short Al_2O_3@ZNR_{es} array reveals a stronger antibacterial activity than long Al_2O_3@ZNR_l after 4 h; top-flat Al_2O_3@HNR_{es} is also of a decreased BCN relative to Al_2O_3@Ti after 2 h. Collectively, at 24 h, top-flat Al_2O_3@HNR_{es} array was measured to have an antibacterial rate of 29% (i.e., the percentage of reduction in BCNs on the array and Al_2O_3@Ti), however, top-sharp Al_2O_3@ZNR_{es} and Al_2O_3@ZNR_l display antibacterial rates as high as ~ 98% and 96%, respectively (Fig. 3b). Such top-sharp Al_2O_3 nanorods derived antibacterial rates are much higher than those derived by top-blunt TiO_2 nanorods [26], even comparable to those derived by ZnO nanorods [27] and graphdiyne-modified TiO_2 nanorods [34], which kill *S. aureus via* the Zn^{2+} release [27] and photo-thermal/dynamic effect [40] besides topography-derived mechano-puncture action. It is suggested that optimizing topographical parameters of nanorods (especially top sharpness) instead of introducing antibacterial components can also achieve strong antibacterial activity.

To identify the antibacterial manner, live/dead fluorescence staining tests of *S. aureus* on the arrays were performed together with Al_2O_3@Ti, as shown in Fig. 3c. Clearly, Al_2O_3@HNR_{es} array keeps all the mounted *S. aureus* to be viable (marked in green color) with the comparable number to Al_2O_3@Ti at 5 min but less than Al_2O_3@Ti at 2, 4 and 24 h, indicating a bacteriostatic (exactly proliferation-inhibited rather than adhesion-inhibited) action of the top-flat array on *S. aureus*. On contrary, although Al_2O_3@ZNR_{es} and Al_2O_3@ZNR_l arrays have the comparable number of viable *S. aureus* to Al_2O_3@HNR_{es} and Al_2O_3@Ti at 5 min, they gradually evoke the mounted *S. aureus* dead (marked in red color) with incubation time and almost completely kill *S. aureus* at 24 h, indicating a bactericidal action of both the top-sharp arrays. Collecting the live/dead staining images with the plate-counting results, it is revealed that the top sharpness of the nanorods plays a critical role in anti-bacteria, and in the case of sharp top, the decrease in nanorod length further enhances bactericidal activity but to a small extent that is ascribed to nanorod length-dependent tortuosity, which is discussed next. In addition, it is needed to point out that the bactericidal rates of the top-sharp nanorods in the present work are higher than that of the nanostructured arrays mentioned in previous work, such as silicon nanocone [48], TiO_2 nanorods [49] and polymer nanopillars [50]. It may be attributed to the much sharper tops of the nanorods and smaller interrod spacing of Al_2O_3@ZNR_{es} and Al_2O_3@ZNR_l compared to the aforementioned nanostructured arrays, which have been demonstrated to enhance bactericidal activity of nanostructures [38].

It has been reported that formation of biofilm is the predominant threat to induce the failure of orthopedic implants [51]. To examine biofilm formation of *S. aureus* after incubating on the arrays and Al_2O_3@Ti for 24 h, crystal violet staining were performed, as shown in Fig. S4. Both the OD values of the stained bacteria on Al_2O_3@Ti and Al_2O_3@HNR_{es} are extremely high, revealing the formation of *S. aureus* biofilm on Al_2O_3@Ti and Al_2O_3@HNR_{es} after 24 h of incubation. On contrary, almost no color appears on Al_2O_3@ZNR_{es} and Al_2O_3@ZNR_l, suggesting no biofilm forming on these arrays, which is further identified the strong bactericidal activity of the top-sharp nanorods.

3.4. Structural evolution of bacteria on the core-shell structured nanorods patterned arrays

To clarify the reasons for bacteriostatic effect of top-flat Al_2O_3@HNR_{es} and bactericidal effect of top-sharp Al_2O_3@ZNR_{es} and Al_2O_3@ZNR_l, the structural evolution of *S. aureus* on these arrays with incubation time was detailedly investigated as shown in Fig. 4. On Al_2O_3@Ti, *S. aureus* appear ball-shaped in morphology with a diameter of ~500 nm throughout the whole incubation periods. Although *S. aureus* on top-flat Al_2O_3@HNR_{es} are still ball-shaped at 5 and 30 min, the nanorods deform bacterial cell envelops at 2 and 4 h (as marked by green arrow in Fig. 4a). Cell envelop deformation is given to inhibit bacterial proliferation [26], consequently leading to reduction of BCNs on Al_2O_3@HNR_{es} compared to Al_2O_3@Ti with incubation time (Fig. 3a and c).

Notably, *S. aureus* secreted EPS is clearly visible on Al_2O_3@HNR_{es}, also on Al_2O_3@ZNR_{es} and Al_2O_3@ZNR_l at 5 min of incubation (as marked by white arrow in Fig. 4a). Owing to the recognition that the longer are nanorods the lower is their bending stiffness [28], EPS-induced adhesive force draws the longer nanorods of Al_2O_3@ZNR_l to bend, as displayed at 30 min for example (Fig. 4 and Fig. S5) and nor do the shorter nanorods of Al_2O_3@HNR_{es} and Al_2O_3@ZNR_{es} throughout the whole incubation periods. Based on the horizontal deflection of the bended nanorods of Al_2O_3@ZNR_l (Fig. S5), the adhesive force of *S. aureus* to Al_2O_3@ZNR_l can be calculated according to Euler-Bernoulli's beam theory using the following equation, as adopted in previous work [52].

$$F = \frac{3EI\delta}{L^3} \quad (1)$$

where F is bacterial adhesive force, δ is horizontal deflection of nanorod top, L is nanorod length, E is Young's modulus of nanorod, and I is area moment. In our work, δ is ~33 nm in average as measured in the SEM images picked from different observation regions (Fig. S5); the nanorod length of Al_2O_3@ZNR_l is ~884 nm. Given that if a coated Al_2O_3 layer is of a thickness lower than 2 nm it would not influence the Young's modulus of a nanorod [53], based on the thickness of amorphous Al_2O_3 shell to be ~1.5 nm, the Young's modulus of Al_2O_3@ZNR_l could be considered the same as ZnO core with a value of 160 GPa [54]. Consequently, the adhesive force of *S. aureus* to Al_2O_3@ZNR_l calculated based on above equation is about 27 nN. It is worth pointing out that the adhesive force of bacteria to their underlying substrate depends on the surface composition, wettability, zeta potential, and roughness of the substrate [52]. Owing to the same surface composition of Al_2O_3, roughness, wettability and zeta potential as well as identical interrod spacing and dimeter of the core-shell structured nanorods (Fig. 2a–c and

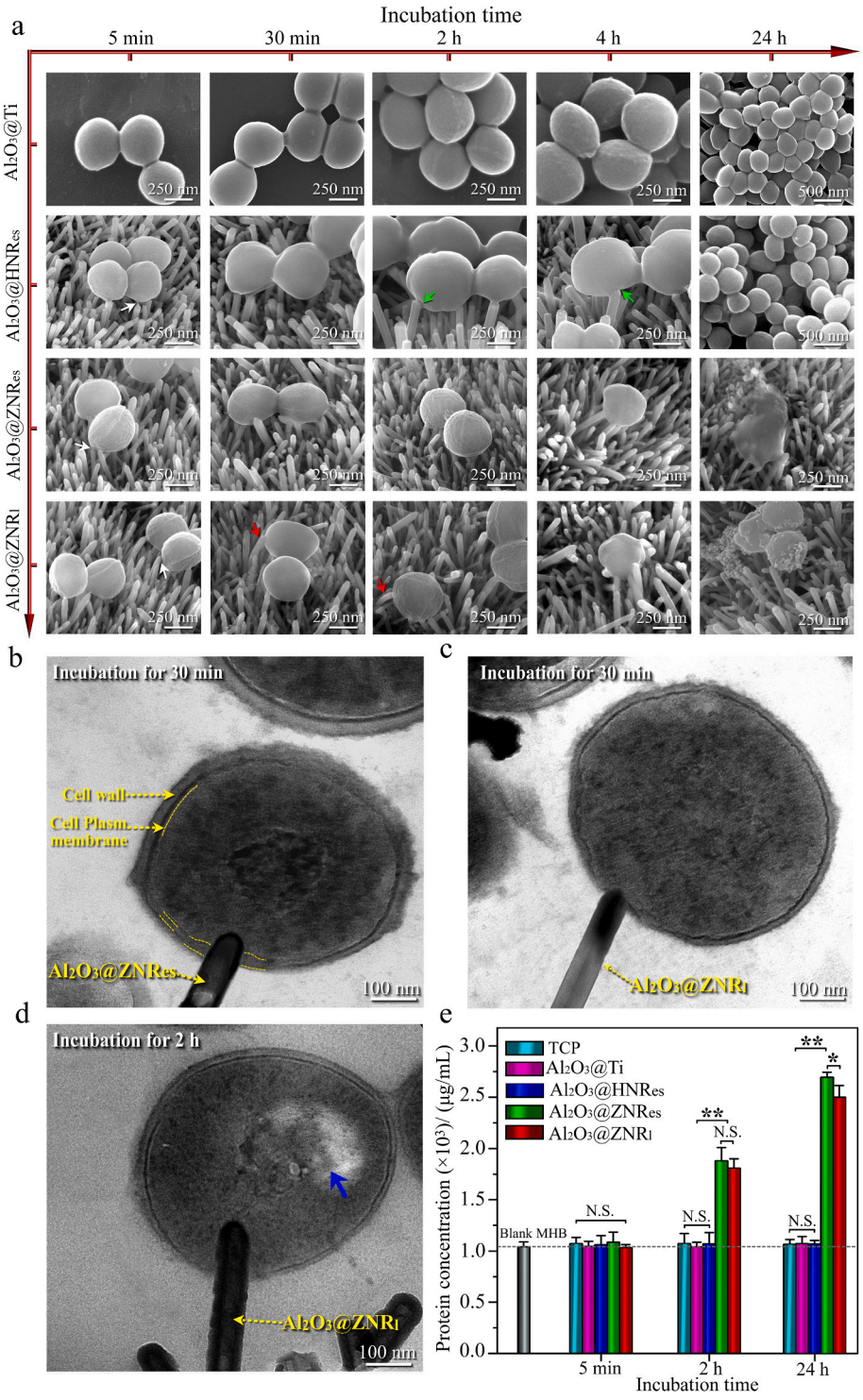

Fig. 4. (a) SEM images of morphological evolution of *S. aureus* cultured on Al_2O_3@Ti and Al_2O_3@HNR_{es}, Al_2O_3@ZNR_{es}, Al_2O_3@ZNR_l for 5 min, 30 min, 2 h, 4 h and 24 h; TEM images of ultrafine structures of *S. aureus* cultured on (b) Al_2O_3@ZNR_{es} and (c) Al_2O_3@ZNR_l for 30 min as well as on (d) Al_2O_3@ZNR_l for 2 h (white arrow: bacteria secreted extracellular polymeric substance; green arrow: cell envelope deformation; red arrow: nanorods bending; blue arrow: electron-lucent region, indicating the leakage of intracellular proteins of bacteria); (e) protein concentrations of the MHB culturing *S. aureus* seeded on Al_2O_3@Ti and Al_2O_3@HNR_{es}, Al_2O_3@ZNR_{es}, Al_2O_3@ZNR_l for 5 min, 2 h, and 24 h, together with the protein concentrations of blank MHB, and the MHB culturing *S. aureus* seeded on tissue culture plate (TCP) as controls. (*$p < 0.05$, **$p < 0.01$, N. S.: no significance).

1b-d), it could be deduced that the adhesive forces of bacteria to Al_2O_3@HNR_{es}, Al_2O_3@ZNR_{es} and Al_2O_3@ZNR_l are essentially equivalent.

Different from only deformation of bacterial cell envelop appearing on top-flat Al_2O_3@HNR_{es} up to 2 h, the adhesive force drives Al_2O_3@ZNR_{es} and Al_2O_3@ZNR_l to wrinkle *S. aureus* surfaces at 5 min, even though the bacteria keep near-spherical shape on these top-sharp nanorods (Fig. 4a). The result indicates that the top-sharp nanorods induce higher stress on cell envelops of the adhered bacteria compared to the top-flat nanorods, owing to the fact that high stress on cell wall can distort the linkage between bacterial outer membrane and peptidoglycan to induce surface wrinkling [55]. At 30 min of incubation, both top-sharp Al_2O_3@ZNR_{es} and Al_2O_3@ZNR_l penetrate into the adhesive bacteria at a depth of ~64 and 26 nm, respectively, as identified by TEM images in Fig. 4b and c. Moreover, the penetration elicits the structural disruption of bacterial cell envelop, which is severer for *S. aureus* on Al_2O_3@ZNR_{es}, showing the thickening of cell envelop adjacent to nanorods (Fig. 4b). The difference in penetration depth of nanorods into *S. aureus* presented by the top-sharp arrays maybe ascribe the difference in nanorod length-dependent tortuosity. When bacterial adhesive force

derives a nanorod bending, the axial component of the adhesive force is seemingly reduced owing to the presence of horizontal component of the force (Fig. S6), leading to a shallower penetration depth of longer Al_2O_3@ZNR_l. The shallower penetration depth of longer Al_2O_3@ZNR_l may lead to a slightly decreased bactericidal rate of Al_2O_3@ZNR_l compared to shorter Al_2O_3@ZNR_{es} against *S. aureus* after a longer incubation term (Fig. 3a and b). With prolonging incubation time to 2 h, Al_2O_3@ZNR_l nanorods are shown to penetrate into *S. aureus* at a great depth of ~125 nm (Fig. 4d). The deepened penetration of the nanorods seriously destroys the integrity of cell envelop (Fig. 4d), resulting in the leakage of intracellular proteins, as identified by the electron-lucent in Fig. 4d and the increase in the total protein concentrations of the resultant MHB in Fig. 4e. The leakage of intracellular proteins induces *S. aureus* collapsing and sinking into the surrounding leaks at 24 h (Fig. 4a). Given that EPS-derived adhesive force of bacteria depends on surface property of substrate [52], gram-negative bacteria, such as *E. coli*, may exhibit comparable adhesive force to these nanorods compared to *S. aureus*; together with the fact of thinner cell wall of *E. coli* [2,34], it can be deduced that top-sharp nanorods are also able to penetrate into *E. coli* to kill them.

Collectively, the aforementioned results reveal that the adhesive force of *S. aureus* drives the top-flat nanorods to deform cell envelop appearing bacteriostatic, but draws the top-sharp nanorods to penetrate into *S. aureus* appearing bactericidal. Considering essentially equivalent adhesive forces of *S. aureus* to Al_2O_3@HNR_{es} and Al_2O_3@ZNR_{es}, the different antibacterial mechanisms of the arrays may originate from the different stresses acting on cell envelops as identified next.

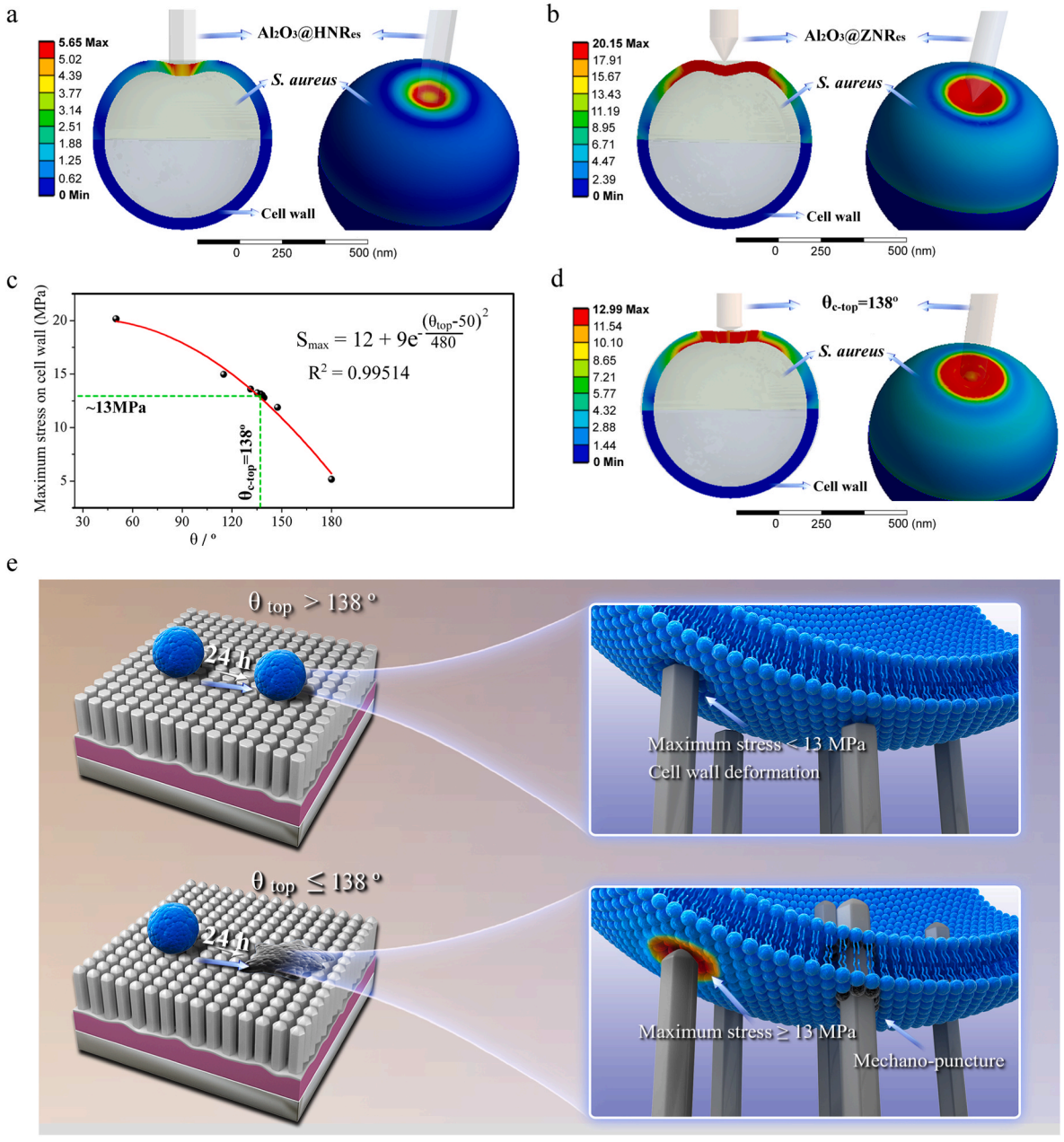

Fig. 5. The finite element-simulated nephograms of stress distribution on cell walls of *S. aureus* on (a) Al_2O_3@HNR_{es} and (b) Al_2O_3@ZNR_{es}; (c) fitting curve of the maximum stress (S_{max}) acting on cell wall *versus* θ_{top} of nanorods obtained using dichotomy and its expression formula; (d) re-simulated nephogram of stress distribution on cell wall of *S. aureus* at θ_{top} of 138°; (e) schematic illustration of the antibacterial mechanisms of nanorods with different top sharpness, showing nanorods to deform cell envelop appearing bacteriostatic at θ_{top} larger than 138°, while to penetrate into *S. aureus* appearing bactericidal at θ_{top} smaller than 138°.

3.5. The finite element simulated stress distribution on cell wall induced by the nanorods with different top sharpness

To quantitatively demonstrate the effect of nanorod top sharpness on the stress acting on cell envelop and to identify the critical top sharpness ($\theta_{c\text{-}top}$) of the nanorods able to penetrate into *S. aureus*, finite element (FE) simulation was carried out on Al_2O_3@HNR_{es} with θ_{top} of 180° and Al_2O_3@ZNR_{es} with θ_{top} of 50°, which have an identical nanorod dimeter and length and almost do not bend under the adhesive force of *S. aureus* throughout the whole incubation periods. Although nanorods density plays a key role in mechano-puncture activity of a nanorods patterned array against bacteria [1], Al_2O_3@HNR_{es} and Al_2O_3@ZNR_{es} exhibit identical interrod spacing and nanorod diameter, which result in a comparable nanorods density of the arrays, excluding its contribution to the different antibacterial activities of these arrays. Moreover, as shown in Fig. 4a, an individual nanorod with sharp top can penetrate into *S. aureus*. Therefore, to simplify the FE model, individual nanorods of Al_2O_3@HNR_{es} and Al_2O_3@ZNR_{es} were used in the FE simulation. Given that bacterial cell wall is a principal stress-bearing and shape-maintaining element relative to membrane [56], bacterial cell envelop can reasonably be simplified to cell wall in our FE model, which involves parameters including the thickness, Young's modulus and ultimate tensile strength (UTS) of *S. aureus* cell wall, internal hydrostatic pressure of *S. aureus*, the applied force of nanorod to cell wall and the θ_{top} of nanorod. As known, the cell wall of *S. aureus* is usually modeled as a thin elastic shell with a thickness of ~35 nm [24,26], the internal fluid in bacteria is usually considered to be incompressible [24] with a constant internal hydrostatic pressure of ~10 atm for *S. aureus* [57], and the Young's modulus and UTS of *S. aureus* cell wall are ~30 MPa and 13 MPa, respectively [58]. The adhesive force of *S. aureus* to each nanorod of Al_2O_3@HNR_{es} and Al_2O_3@ZNR_{es} provides the applied force of a nanorod to cell wall, with a value of ~27 nN as calculated above. Based on these parameters, the stress distribution nephograms on cell walls of *S. aureus* on Al_2O_3@HNR_{es} and Al_2O_3@ZNR_{es} were FE simulated as shown in Fig. 5a and b. Clearly, one of top-flat Al_2O_3@HNR_{es} derives the maximum stress of 5.65 MPa on cell wall (Fig. 5a), quite lower than UTS (13 MPa), resulting in mechano-deformation of *S. aureus* (Fig. 4a), while one of top-sharp Al_2O_3@ZNR_{es} derives the maximum stress of 20.15 MPa on cell wall (Fig. 5b), much higher than UTS, leading to mechano-puncture into *S. aureus* (Fig. 4a). To further identify critical θ_{top}, at which the nanorods-derived maximum stress on cell wall equals to its UTS of 13 MPa, dichotomy of θ_{top} was carried out using 115° (the mean value of 180 and 50°) as a starting point which was substituted into our FE-model to obtain the maximum stress on cell wall at θ_{top} of 115°. Subjecting to such continuous iteration to approach the maximum stress of 13 MPa, critical θ_{top} of the nanorods was drawn to be 138° (Fig. 5c). We re-simulated the stress distribution nephogram on cell wall of *S. aureus* at θ_{top} of 138° subjecting to the applied force of 27 nN using the FE-model, as shown in Fig. 5d. It is revealed that the acting stress on the same position of cell wall and the maximum stress at θ_{top} of 138° are higher than those at 180° but lower than those at 50°. Crucially, we fitted the curve of the maximum stress (S_{max}) acting on cell wall *versus* θ_{top} of the nanorods using dichotomy (Fig. 5c), drawing its expression formula as follow, with the correlation coefficient value R^2 of 0.995:

$$S_{max} = 12 + 19e^{-\frac{(\theta_{top}-50)^2}{480}} \quad (2)$$

which provides the quantitative basis to optimize the top sharpness of nanorods for achieving high efficacy of mechano-puncture into *S. aureus*. Based on the present FE stimulation, it is suggested that driven by the adhesive force of *S. aureus*, the nanorods deform cell envelop appearing bacteriostatic at θ_{top} larger than 138°, while penetrate into *S. aureus* appearing bactericidal at θ_{top} smaller than 138°, as schematically shown in Fig. 5e.

3.6. Anti-bacterial and osseointegrative activities of the coated pillars in vivo

To assay the *in vivo* antibacterial and osseointegrative activities of the arrays, the Al_2O_3@HNR_{es} and Al_2O_3@ZNR_{es} patterned pillars were implanted in *S. aureus*-infected marrow cavities of rat tibias, together with the Al_2O_3@Ti pillars. Fig. 6a and b shows the photographs and corresponding counts of *S. aureus* colonies formed by rolling the implanted pillars on blood agar plates and re-culturing for 24 h. Although an obvious decrease in bacterial amount is displayed on top-flat Al_2O_3@HNR_{es} compared to Al_2O_3@Ti owing to the inhibition of bacterial proliferation, there are still a mass of viable bacteria on Al_2O_3@HNR_{es} at day 3 and week 4 of implantation. Conversely, almost no viable bacteria appear on top-sharp Al_2O_3@ZNR_{es} at day 3 and week 4 of implantation, disclosing the *in vivo* bactericidal rate of Al_2O_3@ZNR_{es} higher than 98%.

Osseointegration is primarily mediated by MSCs [59]. To understand the effect on cells, the arrays together with Al_2O_3@Ti were assessed on the viability and proliferation of rat bone marrow MSCs (rBMSCs) *in vitro* with alamar blue and fluorescent live/dead staining, respectively. Al_2O_3@HNR_{es}, Al_2O_3@ZNR_{es} and Al_2O_3@ZNR_l exhibit the mitochondrial activity of rBMSCs equivalent to each other but higher than Al_2O_3@Ti (Fig. 7a). Moreover, these arrays significantly promote rBMSC adhesion and proliferation compared to planar Al_2O_3@Ti (Fig. 7b), which is ascribed to the role of nanotopography in enhancing the expression of cell integrins and formation of focal adhesions [59–61]. Contrary to the action on *S. aureus*, all the top-flat and top-sharp arrays do not impair rBMSCs, it may be attributed to the following reasons: (1) the Young's modulus of stem cells is three orders lower than that of bacterial cell envelops, ensuring sufficient flexibility of the stem cells to conform to their underlying nanorods without puncture [62,63]; (2) different from the incapable of bacteria to adapt to their underlying substrate, mammalian cells actively sense and respond to their adhered substrate through modulation of their morphology mediated by the cytoskeleton and formation of focal adhesions [49], reducing the nanorods derived stress on cell membrane; (3) the three-dimensional architecture of extracellular matrix that enables rBMSCs to withstand high stress without plastic deformation or rupture [64]. Nevertheless, further investigation are needed to clarify the accurate reasons for the contrary actions on *S. aureus* and rBMSCs induced by the top-sharp nanorods in the present work.

Fig. 6c–f shows the Micro-CT reconstructed images as well as the statistical bone volume fractions, and trabecular number and thickness of new bone surrounding the pillars implanted for 4 weeks. Even in bacteria-infected case, Al_2O_3@ZNR_{es} patterned pillar still induces more pronounced new bone than Al_2O_3@HNR_{es} patterned pillar, while Al_2O_3@Ti pillar rarely induces new bone. This difference is further confirmed by Van Gieson's staining images (Fig. 6g) and the statistical bone-implant contact ratios (Fig. 6h). Top-sharp Al_2O_3@ZNR_{es} patterned pillar shows the quantity of *de novo* bone apposition and bone-implant contact ratio higher than top-flat Al_2O_3@HNR_{es} patterned pillar and much higher than Al_2O_3@Ti pillar. Taken together, top-sharp Al_2O_3@ZNR_{es} array exhibit good *in vitro* viability and proliferation of rBMSCs and strong *in vivo* bactericidal activity, leading to fair osseointegration in *S. aureus*-infected rat tibias.

4. Conclusions

Employing the fabricated three kinds of arrays consisting of Al_2O_3-wraped nanorods, which have nanorod top conical angles of 50 and 180° and nanorod lengths of about 469 and 884 nm, we show that the difference in antibacterial activities of the arrays is dependent on nanorod top sharpness rather than nanorod length without the contributions of chemical components as well as roughness, wettability and zeta potentials. Driven by the EPS-derived equivalent adhesive force of *S. aureus* to the assays, the top-flat nanorods just deform *S. aureus* cell

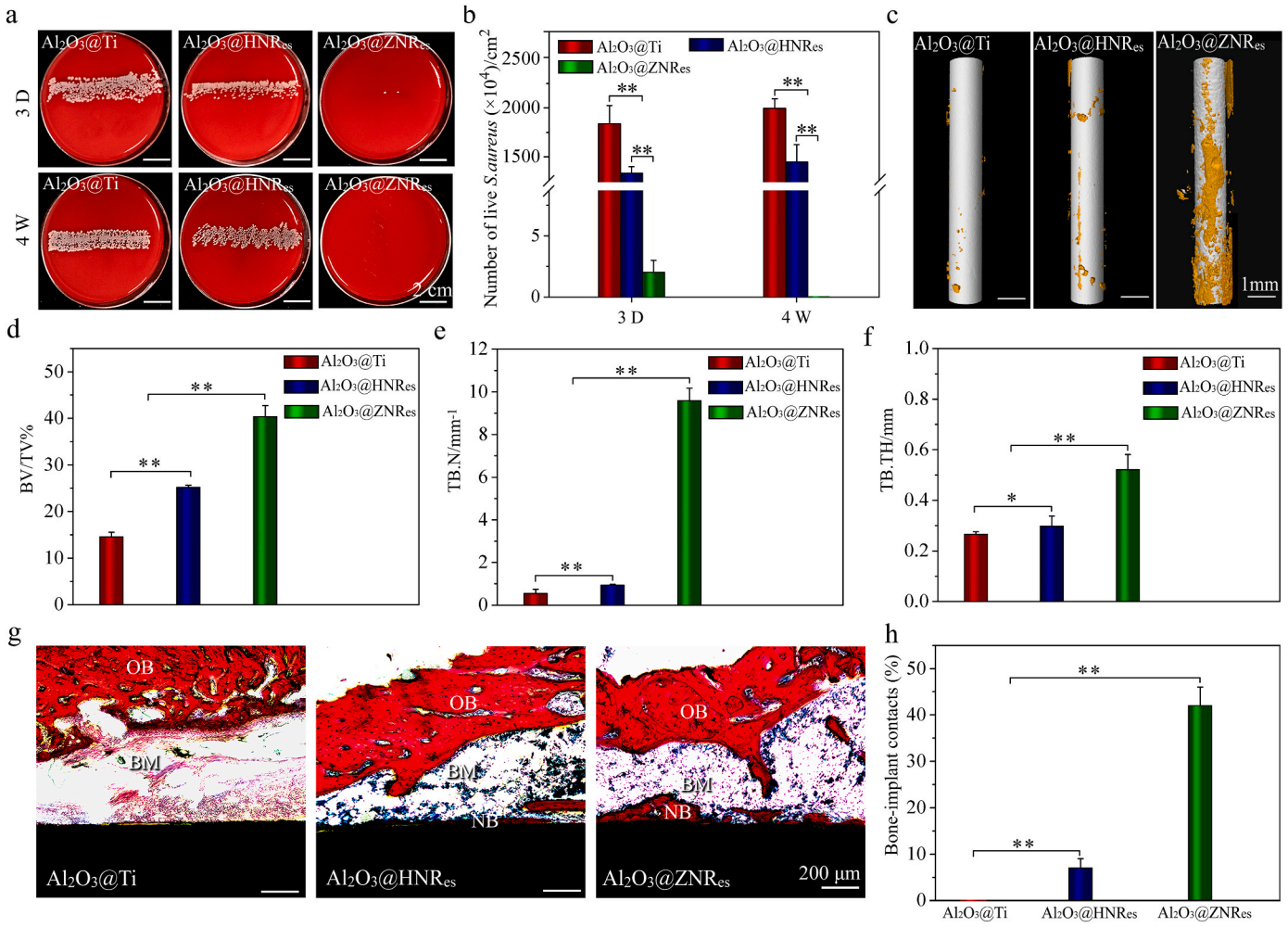

Fig. 6. Histological analyses of Al_2O_3@Ti pillars as well as Al_2O_3@HNR_{es} and Al_2O_3@ZNR_{es} patterned pillars implanted in *S. aureus*-infected marrow cavities of rat tibias for 3 days and 4 weeks: (a) Photographs and (b) the corresponding counts of *S. aureus* colonies formed by rolling the implanted pillars on blood agar plates and re-culturing for 24 h; (c) Micro-CT reconstructed images of the pillars implanted for 4 weeks and quantitation of (d) bone volume fraction (BV/TV %), (e) trabecular number (TB. N) and (f) trabecular thickness (TB. TH) of the peri-implant bone based on Micro-CT assay; (g) Van Gieson's staining images of the pillars implanted for 4 weeks and (h) corresponding bone-implant contacts. Data are presented as mean ± SD, n = 6, (*) $p < 0.05$ and (**) $p < 0.01$.

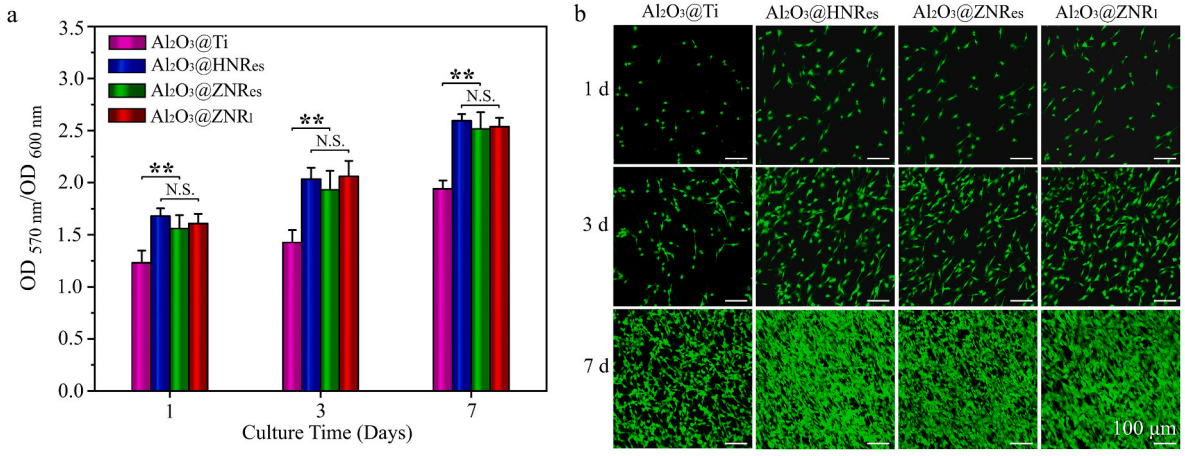

Fig. 7. (a) Metabolic activity and (b) fluorescent live/dead straining images of rBMSCs incubated on Al_2O_3@Ti and Al_2O_3@HNR_{es}, Al_2O_3@ZNR_{es}, Al_2O_3@ZNR_l for 1, 3 and 7 days. (**$p < 0.01$, N. S.: no significance).

envelops, owing to the derived maximum stress (S_{max}) on cell wall to be 5.65 MPa quite lower than the ultimate-tensile-strength (UTS) of cell wall, and show an antibacterial rate of 29% against *S. aureus* in proliferation-inhibited manner. However, the top-sharp nanorods penetrate into *S. aureus*, owing to the derived S_{max} of 20.15 MPa much higher than UTS, and show an antibacterial rate of 98% for the shorter

and 96% for the longer in bactericidal manner. Moreover, the relationship between the top conical angle and nanorod derived S_{max} on cell wall is formularized, and a critical top conical angle of 138° is calculated for the nanorods able to penetrate into *S. aureus* based on the FE stimulation in the present work. Furthermore, the top-sharp but short nanorods patterned array exhibits good *in vitro* proliferative ability of rBMSCs and strong bactericidal activity in *S. aureus*-infected rat tibias, and thus simultaneously shows fair osseointegration. Our work provides quantitative basis for optimizing top sharpness of nanorods to achieve mechano-puncture derived strong bactericidal efficacy without introducing chemical bactericides to impair osseointegration.

CRediT authorship contribution statement

Jing Ye: Methodology, Investigation, Data curation, Visualization, Writing – original draft, and. **Bo Li:** Methodology, Investigation, Data curation, Visualization, Writing – original draft. **Yufeng Zheng:** Supervision. **Shuilin Wu:** Supervision, and. **Dafu Chen:** Supervision. **Yong Han:** Conceptualization, Funding acquisition, Supervision, Writing – review & editing.

Declaration of competing interest

The authors declare that they have no known competing financial interests or personal relationships that could have appeared to influence the work reported in this paper.

Acknowledgements

The authors appreciate the National Natural Science Foundation of China (Grant number 51631007, 51971171 and 3700860), and the joint project of Xi'an Jiaotong University and Beijing Research Institute of Traumatology and Orthopaedics (Contract No. 202012443) for financially supporting this work.

Appendix A. Supplementary data

Supplementary data to this article can be found online at https://doi.org/10.1016/j.bioactmat.2021.11.028.

References

[1] K. Modaresifar, S. Azizian, M. Ganjian, L.E. Fratila-Apachitei, A.A. Zadpoor, Bactericidal effects of nanopatterns: a systematic review, Acta Biomater. 83 (2019) 29–36.
[2] D.P. Linklater, V.A. Baulin, S. Juodkazis, R.J. Crawford, P. Stoodley, E.P. Ivanova, Mechano -bactericidal actions of nanostructured surfaces, Nat. Rev. Microbiol. 19 (2020) 8–22.
[3] S. Bakhshandeh, Z. Gorgin-Karaji, K. Lietaert, A.C. Fluit, C.H.E. Boell, H.C. Vogely, T. Vermonden, W.E. Hennink, H. Weinans, A.A. Zadpoor, Y.S. Amin, Simultaneous delivery of multiple antibacterial agents from additively manufactured porous biomaterials to fully eradicate planktonic and adherent *Staphylococcus aureus*, ACS Appl. Mater. Interfaces 9 (2017) 25691–25699.
[4] M. Fathi, B. Akbari, A. Taheriazam, Antibiotics drug release controlling and osteoblast adhesion from titania nanotubes arrays using silk fibroin coating, Mater. Sci. Eng. C 103 (2019) 109743.
[5] J. Hirschfeld, E.M. Akinoglu, D.C. Wirtz, A. Hoerauf, I. Bekeredjian-Ding, S. Jepsen, E.-M. Haddouti, A. Limmer, M. Giersig, Long-term release of antibiotics by carbon nanotube-coated titanium alloy surfaces diminish biofilm formation by *Staphylococcus epidermidis*, Nanomed. Nanotechnol. 13 (2017) 1587–1593.
[6] J. Ye, B. Li, M. Li, Y. Zheng, S. Wu, Y. Han, ROS induced bactericidal activity of amorphous Zn-doped titanium oxide coatings and enhanced osseointegration in bacteria-infected rat tibias, Acta Biomater. 107 (2020) 313–324.
[7] J. Zhou, B. Li, L. Zhao, L. Zhang, Y. Han, F-doped micropore/nanorod hierarchically patterned coatings for improving antibacterial and osteogenic activities of bone implants in bacteria-infected cases, ACS Biomater. Sci. Eng. 3 (2017) 1437–1450.
[8] L. Zhang, J. Guo, T. Yan, Y. Han, Fibroblast responses and antibacterial activity of Cu and Zn co-doped TiO_2 for percutaneous implants, Appl. Surf. Sci. 434 (2018) 633–642.
[9] P. Makvandi, C.y. Wang, E.N. Zare, A. Borzacchiello, L.n. Niu, F.R. Tay, Metal-based nanomaterials in biomedical applications: antimicrobial activity and cytotoxicity aspects, Adv. Funct. Mater. 30 (2020) 1910021.
[10] Y. Zhang, L. Zhang, B. Li, Y. Han, Enhancement in sustained release of antimicrobial peptide from dual-diameter-structured TiO_2 nanotubes for long-lasting antibacterial activity and cytocompatibility, ACS Appl. Mater. Interfaces 9 (2017) 9449–9461.
[11] T.S. Crofts, A.J. Gasparrini, G. Dantas, Next-generation approaches to understand and combat the antibiotic resistome, Nat. Rev. Microbiol. 15 (2017) 422–434.
[12] K.A. Brogden, Antimicrobial peptides: pore formers or metabolic inhibitors in bacteria? Nat. Rev. Microbiol. 3 (2005) 238–250.
[13] N. Duewelhenke, O. Krut, P. Eysel, Influence on mitochondria and cytotoxicity of different antibiotics administered in high concentrations on primary human osteoblasts and cell lines, Antimicrob. Agents Chemother. 51 (2007) 54–61.
[14] M.C. Morales-Alvarez, Nephrotoxicity of antimicrobials and antibiotics, Adv. Chron. Kidney Dis. 27 (2020) 31–37.
[15] M. Rana, A.K. Sharma, Cu and Zn interactions with Aβ peptides: consequence of coordination on aggregation and formation of neurotoxic soluble Aβ oligomers, Metallomics 11 (2019) 64–84.
[16] Y. Ren, H. Liu, X. Liu, Y. Zheng, Z. Li, C. Li, K.W. Yeung, S. Zhu, Y. Liang, Z. Cui, S. Wu, Photoresponsive materials for antibacterial applications, Cell Rep. Phys. Sci. 1 (2020) 100245.
[17] B. Sun, X. Zhen, X. Jiang, Development of mesoporous silica-based nanoprobes for optical bioimaging applications, Biomater. Sci. 9 (2021) 3603.
[18] Q. Wu, L. Tan, X. Liu, Z. Li, Y. Zhang, Y. Zheng, Y. Liang, Z. Cui, S. Zhu, S. Wu, The enhanced near-infrared photocatalytic and photothermal effects of MXene-based heterojunction for rapid bacteria-killing, Appl. Catal. B Environ. 297 (2021) 120500.
[19] Y. Tian, Y. Li, J. Liu, Y. Lin, J. Jiao, B. Chen, W. Wang, S. Wu, C. Li, Photothermal therapy with regulated Nrf2/NF-κB signaling pathway for treating bacteria-induced periodontitis, Bioact. Mater. 9 (2022) 428–445.
[20] H. Liu, J. Li, X. Liu, Z. Li, Y. Zhang, Y. Liang, Y. Zheng, S. Zhu, Z. Cui, S. Wu, Photo-sono interfacial engineering exciting the intrinsic property of herbal nanomedicine for rapid broad-spectrum bacteria killing, ACS Nano 15 (2021) 18505–18519.
[21] C. Lia, J. Wang, Y. Wang, H. Gao, G. Wei, Y. Huang, H. Yu, Y. Gan, Y. Wang, L. Mei, H. Chen, H. Hu, Z. Zhang, Y. Jin, Recent progress in drug delivery, Acta Pharm. Sin. B 9 (2019) 1145–1162.
[22] E.P. Ivanova, J. Hasan, H.K. Webb, V.K. Truong, G.S. Watson, J.A. Watson, V. A. Baulin, S. Pogodin, J.Y. Wang, M.J. Tobin, C. Lobbe, R.J. Crawford, Natural bactericidal surfaces: mechanical rupture of *Pseudomonas aeruginosa* cells by cicada wings, Small 8 (2012) 2489–2494.
[23] E.P. Ivanova, J. Hasan, H.K. Webb, G. Gervinskas, S. Juodkazis, V.K. Truong, A. H. Wu, R.N. Lamb, V.A. Baulin, G.S. Watson, J.A. Watson, D.E. Mainwaring, R. J. Crawford, Bactericidal activity of black silicon, Nat. Commun. 4 (2013) 2838.
[24] A. Valiei, N. Lin, J.-F. Bryche, G. McKay, M. Canva, P.G. Charette, D. Nguyen, C. Moraes, N. Tufenkji, Hydrophilic mechano-bactericidal nanopillars require external forces to rapidly kill bacteria, Nano Lett. 20 (2020) 5720–5727.
[25] M.N. Dickson, E.I. Liang, L.A. Rodriguez, N. Vollereaux, A.F. Yee, Nanopatterned polymer surfaces with bactericidal properties, Biointerphases 10 (2015), 021010.
[26] J. Jenkins, J. Mantell, C. Neal, A. Gholinia, P. Verkade, A.H. Nobbs, B. Su, Antibacterial effects of nanopillar surfaces are mediated by cell impedance, penetration and induction of oxidative stress, Nat. Commun. 111 (2020) 626.
[27] J. Li, L. Tan, X. Liu, Z. Cui, X. Yang, K.W.K. Yeung, P.K. Chu, S. Wu, Balancing bacteria-osteoblast competition through selective physical puncture and biofunctionalization of ZnO/polydopamine/arginine-glycine-aspartic acid-cysteine nanorods, ACS Nano 11 (2017) 11250–11263.
[28] D.P. Linklater, M. De Volder, V.A. Baulin, M. Werner, S. Jessl, M. Golozar, L. Maggini, S. Rubanov, E. Hanssen, S. Juodkazis, E.P. Ivanova, High aspect ratio nanostructures kill bacteria via storage and release of mechanical energy, ACS Nano 12 (2018) 6657–6667.
[29] S. Pogodin, J. Hasan, V.A. Baulin, H.K. Webb, V.K. Truong, T.H. Phong Nguyen, V. Boshkovikj, C.J. Fluke, G.S. Watson, J.A. Watson, R.J. Crawford, E.P. Ivanova, Biophysical model of bacterial cell interactions with nanopatterned cicada wing surfaces, Biophys. J. 104 (2013) 835–840.
[30] F. Xue, J. Liu, L. Guo, L. Zhang, Q. Li, Theoretical study on the bactericidal nature of nanopatterned surfaces, J. Theor. Biol. 385 (2015) 1–7.
[31] C.D. Bandara, S. Singh, I.O. Afara, A. Wolff, T. Tesfamichael, K. Ostrikov, A. Oloyede, Bactericidal effects of natural nanotopography of dragonfly wing on escherichia coli, ACS Appl. Mater. Interfaces 9 (2017) 6746–6760.
[32] F. Hizal, C.-H. Choi, H.J. Busscher, H.C. van der Mei, Staphylococcal adhesion, detachment and transmission on nanopillared Si surfaces, ACS Appl. Mater. Interfaces 8 (2016) 30430–30439.
[33] Y. Chen, A.K. Harapanahalli, H.J. Busscher, W. Norde, H.C. van der Mei, Nanoscale cell wall deformation impacts long-Range bacterial adhesion forces on surfaces, Appl. Environ. Microbiol. 80 (2014) 637.
[34] S.M. Kelleher, O. Habimana, J. Lawler, B. O R, S. Daniels, E. Casey, A. Cowley, Cicada wing surface topography: an investigation into the bactericidal properties of nanostructural features, ACS Appl. Mater. Interfaces 8 (2016) 14966–14974.
[35] J. Hasan, S. Raj, L. Yadav, K. Chatterjee, Engineering a nanostructured "super surface" with superhydrophobic and superkilling properties, RSC Adv. 5 (2015) 44953–44959.
[36] L.D. Kitara, A.D. Anywar, D. Acullu, E. Odongo-Aginya, J. Aloyo, M. Fendu, Antibiotic susceptibility of *Staphylococcus aureus* in suppurative lesions in Lacor Hospital, Uganda, Afr. Health Sci. 1 (2011) 34–39.
[37] K. Modaresifar, L.B. Kunkels, M. Ganjian, N. Tumer, C.W. Hagen, L.G. Otten, P. L. Hagedoorn, L. Angeloni, M.K. Ghatkesar, L.E. Fratila-Apachitei, A.A. Zadpoor, Deciphering the roles of interspace and controlled disorder in the bactericidal properties of nanopatterns against *Staphylococcus aureus*, Nanomaterials 10 (2020) 347.

[38] M. Michalska, F. Gambacorta, R. Divan, I.S. Aranson, A. Sokolov, P. Noirot, P. D. Laible, Tuning antimicrobial properties of biomimetic nanopatterned surfaces, Nanoscale 10 (2018) 6639–6650.
[39] W. Wang, P. Pei, Z. Chu, B. Chen, H. Qian, Z. Zha, W. Zhou, T. Liu, M. Shao, H. Wang, Bi_2S_3 coated Au nanorods for enhanced photodynamic and photothermal antibacterial activities under NIR light, Chem. Eng. J. 397 (2020) 125488.
[40] R. Wang, M. Shi, F. Xu, Y. Qiu, P. Zhang, K. Shen, Q. Zhao, J. Yu, Y. Zhang, Graphdiyne- modified TiO_2 nanofibers with osteoinductive and enhanced photocatalytic antibacterial activities to prevent implant infection, Nat. Commun. 11 (2020) 4465.
[41] J. Zhou, B. Li, S. Lu, L. Zhang, Y. Han, Regulation of osteoblast proliferation and differentiation by interrod spacing of Sr-HA nanorods on microporous titania coatings, ACS Appl. Mater. Interfaces 5 (2013) 5358–5365.
[42] V.K. Truong, R. Lapovok, Y.S. Estrin, S. Rundell, J.Y. Wang, C.J. Fluke, R. J. Crawford, E.P. Ivanova, The influence of nano-scale surface roughness on bacterial adhesion to ultrafine-grained titanium, Biomaterials 31 (2010) 3674–3683.
[43] V. Fröjd, L. Chávez de Paz, M. Andersson, A. Wennerberg, J.R. Davies, G. Svensäter, In situ analysis of multispecies biofilm formation on customized titanium surfaces, Mol. Oral Microbiol. 26 (2011) 241–252.
[[4][4]] X.-Q. Dou, D. Zhang, C. Feng, L. Jiang, Bioinspired hierarchical surface structures with tunable wettability for regulating bacteria adhesion, ACS Nano 9 (2015) 10664–10672.
[45] Y. Lai, J. Huang, Z. Cui, M. Ge, K.-Q. Zhang, Z. Chen, L. Chi, Recent advances in TiO_2-based nanostructured surfaces with controllable wettability and adhesion, Small 12 (2016) 2203–2224.
[46] S. Spriano, V. Sarath Chandra, A. Cochis, F. Uberti, L. Rimondini, E. Bertone, A. Vitale, C. Scolaro, M. Ferrari, F. Cirisano, G. Gautier di Confiengo, S. Ferraris, How do wettability, zeta potential and hydroxylation degree affect the biological response of biomaterials? Mater. Sci. Eng. C 74 (2017) 542–555.
[47] Y. Yuan, M.P. Hays, P.R. Hardwidge, J. Kim, Surface characteristics influencing bacterial adhesion to polymeric substrates, RSC Adv. 7 (2017) 14254–14261.
[48] D.P. Linklater, H.K.D. Nguyen, C.M. Bhadra, S. Juodkazis, E.P. Ivanova, Influence of nanoscale topology on bactericidal efficiency of black silicon surfaces, Nanotechnology 28 (2017) 245301.
[49] J. Hasan, S. Jain, K. Chatterjee, Nanoscale topography on black titanium imparts multibiofunctional properties for orthopedic applications, Sci. Rep. 7 (2017) 41118.
[50] S. Wu, F. Zuber, K. Maniura-Weber, J. Brugger, Q. Ren, Nanostructured surface topographies have an effect on bactericidal activity, J. Nanobiotechnol. 16 (2018).
[51] N. Høiby, T. Bjarnsholt, M. Givskov, S. Molin, O. Ciofu, Antibiotic resistance of bacterial biofilms, Int. J. Antimicrob. Agents 35 (2010) 322–332.
[52] A. Elbourne, J. Chapman, A. Gelmi, D. Cozzolino, R.J. Crawford, V.K. Truong, Bacterial-nanostructure interactions: the role of cell elasticity and adhesion forces, J. Colloid Interface Sci. 546 (2019) 192–210.
[53] Y. Chen, Q. Gao, Y. Wang, X. An, X. Liao, Y.-W. Mai, H.H. Tan, J. Zou, S.P. Ringer, C. Jagadish, Determination of Young's modulus of ultrathin nanomaterials, Nano Lett. 15 (2015) 5279–5283.
[54] C.Q. Chen, Y. Shi, Y.S. Zhang, J. Zhu, Y.J. Yan, Size dependence of Young's modulus in ZnO nanowires, Phys. Rev. Lett. 96 (2006), 075505.
[55] D. Greif, D. Wesner, J. Regtmeier, D. Anselmetti, High resolution imaging of surface patterns of single bacterial cells, Ultramicroscopy 110 (2010) 1290–1296.
[56] D.-J. Scheffers, M.G. Pinho, Bacterial cell wall synthesis: new insights from localization studies, Microbiol. Mol. Biol. Rev. 69 (2005) 585.
[57] E.R. Rojas, K.C. Huang, Regulation of microbial growth by turgor pressure, Curr. Opin. Microbiol. 42 (2018) 62–70.
[58] J.J. Thwaites, U.C. Surana, Mechanical properties of *Bacillus subtilis* cell walls: effects of removing residual culture medium, J. Bacteriol. 173 (1991) 197–203.
[59] J. Zhou, B. Li, Y. Han, L. Zhao, The osteogenic capacity of biomimetic hierarchical micropore/nanorod-patterned Sr-HA coatings with different interrod spacings, Nanomedicine 12 (2016) 1161–1173.
[60] J. Zhou, Y. Han, S. Lu, Direct role of interrod spacing in mediating cell adhesion on Sr-HA nanorod-patterned coatings, Int. J. Nanomed. 9 (2014) 1243–1260.
[61] J. Zhou, L. Zhao, B. Li, Y. Han, Nanorod diameter modulated osteogenic activity of hierarchical micropore/nanorod-patterned coatings via a Wnt/β-catenin pathway, Nanomedicine 14 (2018) 1719–1731.
[62] N.I. Nikolaev, T. Muller, D.J. Williams, Y. Liu, Changes in the stiffness of human mesenchymal stem cells with the progress of cell death as measured by atomic force microscopy, J. Biomech. 47 (2014) 625–630.
[63] H.H. Tuson, Measuring the stiffness of bacterial cells from growth rates in hydrogels of tunable elasticity, Mol. Microbiol. 84 (2012) 874–891.
[64] L.D. Muiznieks, F.W. Keeley, Molecular assembly and mechanical properties of the extracellular matrix: a fibrous protein perspective, Biochim. Biophys. Acta 1832 (2013) 866–875.